Yao *et al. PhotoniX* (2022)3:23
https://doi.org/10.1186/s43074-022-00069-x

PhotoniX

RESEARCH Open Access

Plasmonic anapole metamaterial for refractive index sensing

Jin Yao[1†], Jun-Yu Ou[2†], Vassili Savinov[2], Mu Ku Chen[1,3,4], Hsin Yu Kuo[2], Nikolay I. Zheludev[2,5*] and Din Ping Tsai[1,3,4*]

† These authors contributed equally to this work.

*Correspondence:
Nikolay I. Zheludev
zheludev@soton.ac.uk
Din Ping Tsai
dptsai@cityu.edu.hk

Full list of author information is available at the end of the article

Abstract

Electromagnetic anapole mode is a nonradiative state of light originating from the deconstructive interference of radiation of the oscillating electric and toroidal dipole moments. The high quality anapole-related resonances can be used in enhancing nonlinear electromagnetic properties of materials and in sensor applications. In this work, we experimentally demonstrate plasmonic anapole metamaterial sensor of environmental refractive index in the optical part of the spectrum. Our results show that the sensor exhibits high sensitivity to the ambient refractive index at the level of 330 nm/RIU and noise floor of 8.7×10^{-5} RIU. This work will pave the way for applications of anapole metamaterials in biosensing and spectroscopy.

Keywords Plasmonic metamaterial, Electromagnetic anapole, Refractive index sensor, Vertical split-ring resonator, Toroidal dipole

Introduction

Refractive index sensing has attracted extensive attention due to a wide range of chemical and biomedical applications [1, 2]. In recent years, plasmonic metamaterials and metasurfaces have emerged as powerful candidates for novel refractive index sensors [3–7]. They possess preeminent capabilities of confining the electromagnetic field at the nanoscale and enhancing the interactions between light and matter, providing high sensitivity to the ambient refractive index variations [8, 9]. Propagating surface plasmon polariton (SPP) and localized surface plasmon resonance (LSPR) are among the most common plasmonic refractive index sensing techniques [10–12]. By carefully engineering and optimizing the nanostructure designs, performant plasmonic sensors with high sensitivity, high figure-of-merit (FOM) and low detection limit have been achieved [13–15]. Beyond this, the research attention has focused on the interplays between resonant modes, such as Fano resonances and quasi-bound states in the continuum. Excellent near-field enhancement and Q factor have been demonstrated, potentially enabling great performance in label-free and real-time sensing applications [16–21].

Electromagnetic anapole mode is a nonradiative resonance that arises as a result of the destructive interference between electric dipole (ED) and toroidal dipole (TD) moments

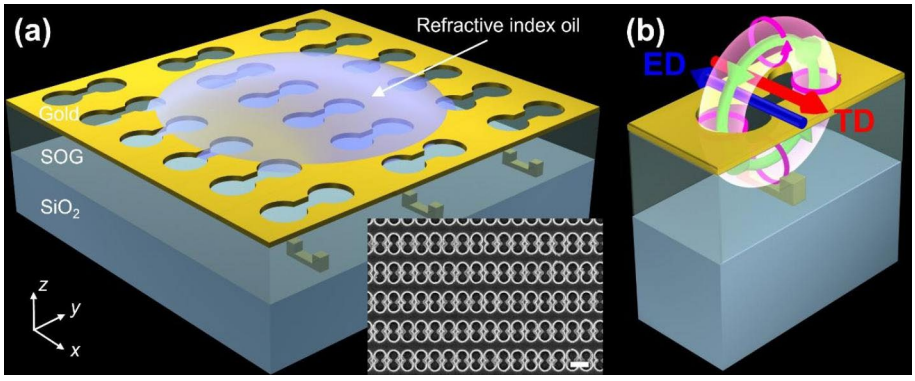

Fig. 1 (a) Schematic diagram of the proposed anapole metamaterial array for refractive index sensing. The inset is the top-view scanning electron microscope image of the fabricated sample. The scale bar is 500 nm. (b) Schematic depiction for the excited anapole mode, which originates from the destructive interference between electric dipole (blue arrow) and toroidal dipole (red arrow with pink torus and green circulating magnetic field) moments

with the same intensity and opposite phase in the far-field [22, 23]. The anapole excitation was first experimentally observed within engineered composite metallic metamaterials at microwave frequency [24]. It was then extended to plasmonic and dielectric metamaterials and metasurfaces in the infrared [25–28]. The generalizations of the electric anapole modes such as the high-order anapole states and the magnetic counterparts have also been studied [29]. The defining nonradiating condition of the anapole relies on the fine balance between the constituent electric dipole and toroidal dipole excitations. Consequently, such excitations are expected to be highly sensitive to external perturbations including variations in the ambient refractive index [30–32]. Compared with conventional dipole modes with low transmission, anapole modes can acquire the effective transmission channel due to the nonradiative property, which is beneficial to practical low-loss sensors [25, 33]. Leveraging this intuition, various enhanced anapole modes and their great sensing performance have been demonstrated in dielectric nanostructures with high refractive index. In contrast, few studies have touched on plasmonic anapole sensing so far, and the experimental demonstration of the plasmonic anapole metamaterial sensor remains unexplored in the optical part of the spectrum. [34–38].

In this work, we experimentally demonstrate plasmonic anapole sensor for refractive index sensing in the optical part of spectrum. By comparing the electromagnetic responses of electric dipole and toroidal dipole, we investigate the physical mechanism of the anapole excitation. Due to the effective coupling between two components, we acquire a higher field enhancement and a narrower linewidth of the whole plasmonic anapole metamaterial, which can improve the refractive index sensing performance. We further numerically and experimentally demonstrate the high sensitivity of the plasmonic refractive index sensor. Simultaneously, we demonstrate tuning of the anapole resonance through control of the ambient refractive index.

Results and discussion

Figure 1a depicts the schematic diagram of the proposed plasmonic anapole metamaterial, which consists of a planar array of vertical split-ring resonators suspended in a spin on glass layer and covered with a dumbbell-perforated gold film. The perforations (apertures) in the gold film are aligned to the vertical split-ring resonators. The inset of Fig. 1a shows the top-view scanning electron microscope image of the fabricated sample.

More details of the fabrication process and scanning electron microscope images can be found in Methods and Supplementary Information. With normal x-polarized plane wave illuminating, circulating currents (pink arrows) in two circular apertures and the vertical split-ring resonator can be induced, which can generate the circulating magnetic field (green arrow) and subsequently excite the x-directed toroidal dipole moments (red arrow) [39, 40], as shown in Fig. 1b. The $-x$-directed electric dipole moments can also be excited due to the charge oscillations at two central edges of the apertures. When two dipole excitations possess the same intensity but are out of phase, the destructive interference between them leads to the anapole mode, accompanied by the strong field confinement and vanishing far-field radiation.

To elaborate on the physical mechanism of the plasmonic anapole metamaterial, we first investigate its two components, the upper dumbbell-perforated gold film and the lower vertical split-ring resonator, whose schematic diagrams of configuration are shown in Fig. 2a and e, respectively. Figure 2b gives the transmission and reflection spectra of the dumbbell-perforated gold film placed on the dielectric substrate. A transmission peak of more than 90% can be observed at resonant wavelength $\lambda = 1608$ nm. According to the multipole decomposition (see Supplementary Information for details) in Fig. 2c, this resonant mode is mainly contributed by the electric dipole and toroidal dipole moments, accompanied by a weak magnetic quadrupole (MQ) contribution. Although electric dipole and toroidal dipole moments have a similar amplitude near the resonant wavelength, their phase difference is not close to π, so the resonance here is intrinsically a hybrid mode instead of an anapole mode. The yz-plane field distributions normalized to the incident wave amplitude, at the resonant wavelength, are plotted in Fig. 2d. An electric hotspot emerges at the center of two apertures and a circulating magnetic field (white dashed arrows) can be observed, which exhibits the characteristics of both electric dipole and toroidal dipole distributions and thus offers the possibility for anapole excitation [25].

Figure 2f shows the spectra of the vertical split-ring resonator suspended in a spin on glass layer. A transmission dip of around 10% indicates that the resonance is excited at wavelength $\lambda = 1892$ nm. The main components of the excitation are a dominant electric dipole moment as well as weak magnetic dipole (MD) and electric quadrupole (EQ) moments, as shown in Fig. 2 g. This configuration does not constitute an anapole mode in the desired spectral range because the similar amplitude and the opposite phase for electric dipole and toroidal dipole moments do not appear simultaneously. The normalized field distributions are presented in Fig. 2 h. The electric hotspot and magnetic hotspot can be found in the center of the vertical split-ring resonator, indicating the excitations of both electric dipole and magnetic dipole moments [41–44]. The electric hotspot of the vertical split-ring resonator can effectively overlap that of the dumbbell-perforated gold film, and the magnetic hotspot of the vertical split-ring resonator can boost the circulating magnetic field of the dumbbell-perforated gold film due to their similar orientations in the spin on glass layer. Although the anapole mode cannot be directly acquired in the single component, combining two components provides the conditions for the anapole excitation. Consequently, combing these two components can generate efficient coupling between them and enhance the electric dipole and toroidal dipole moments simultaneously, which is expected to provide the opportunity for a strong anapole response.

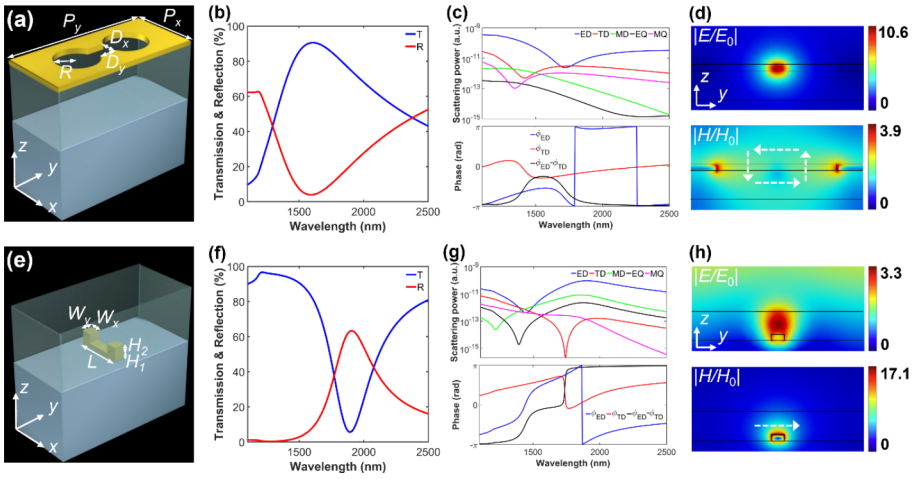

Fig. 2 Electromagnetic responses of two components of the plasmonic anapole metamaterial. (a) Schematic diagram of the configuration, (b) transmission (blue curve) and reflection (red curve) spectra, (c) multipole decomposition and phases of electric dipole and toroidal dipole moments, and (d) normalized *yz*-plane electric field and magnetic field distributions of the dumbbell-perforated gold film placed on the dielectric substrate. The field distribution is extracted from the corresponding resonant wavelength. White dashed arrows depict the orientations of the magnetic field. (e), (f), (g) and (h) Those for the vertical split-ring resonator suspended in a spin on glass layer. Feature sizes: $P_x = 380$ nm, $P_y = 820$ nm, $R = 130$ nm, $D_x = 65$ nm, $D_y = 60$ nm, $L = 270$ nm, $W_x = 60$ nm, $W_y = 60$ nm, $H_1 = 30$ nm, $H_2 = 55$ nm, and thicknesses of the perforated gold film and the spin on glass film are 30 and 135 nm, respectively

To verify the analysis above, we experimentally and numerically demonstrate the plasmonic anapole metamaterial combining both dumbbell-perforated gold film and vertical split-ring resonator components. Since the device performance is dominated by the physical mechanism of anapole mode instead of optimized parameters, the geometric parameters selection is mainly based on the mechanism of anapole excitation and the fabrication precision. The experimentally measured transmission and reflection spectra are plotted in Fig. 3a. The transmission peak representing the resonance can be observed at wavelength $\lambda = 1340$ nm, showing a blue shift compared to the resonant wavelengths of two components (1608 and 1892 nm). That is because the involvement of the other component introduces not only new material but also effective coupling between two components. The measured line shape of the transmission and reflection spectra agree well with the simulated results in Fig. 3b. The slight difference in the peak values of transmission and reflection, as well as a broader line width in the experimental measurements, are expected due to inevitable variations in metamaterial dimensions and imperfections with the fabricated sample.

Figure 3c and d depict the multipole decomposition and phases of electric dipole and toroidal dipole moments of the plasmonic anapole metamaterial, respectively. Electric dipole and toroidal dipole moments have similar amplitudes and approximately opposite phases at the wavelength around $\lambda = 1340$ nm (grey dotted lines), implying the effective excitation of the anapole mode. It is interesting to point out that the slight deviation of phase difference from -π results from the involved additional loss of gold (See Methods and Supplementary Information), which will not influence the mechanism of anapole excitation. The electromagnetic field distributions are given in Fig. 3e. The electric hotspot is located at the center of dumbbell-perforated gold film and the magnetic hotspots emerge at two aperture edges and in the center of the vertical split-ring

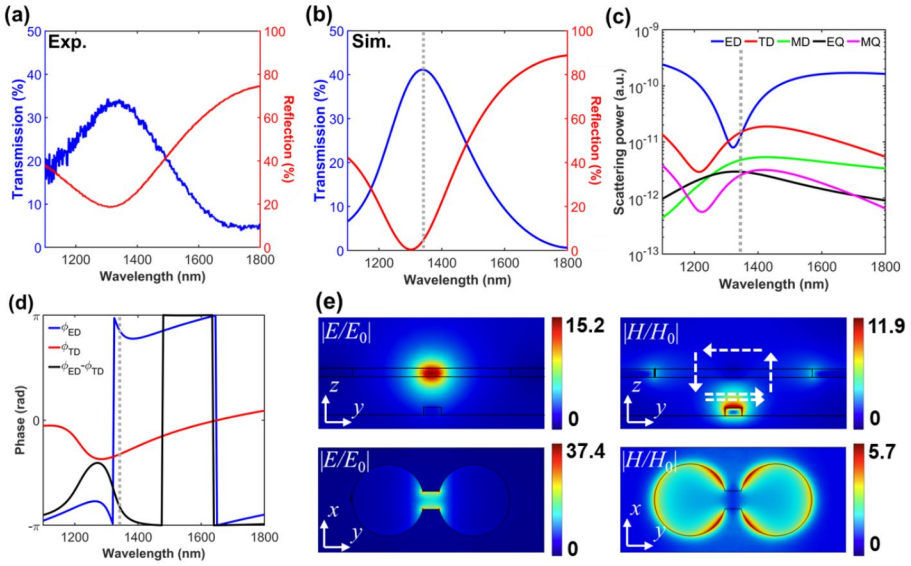

Fig. 3 Electromagnetic responses of the plasmonic anapole metamaterial. (a) Measured and (b) simulated transmission (blue curve) and reflection (red curve) spectra, (c) multipole decomposition, (d) phases of electric dipole and toroidal dipole moments, and (e) normalized electric field and magnetic field distributions of the plasmonic anapole metamaterial in the *yz*-plane and the *xy*-plane. Grey dotted lines in Fig. 3b-d denote the resonant wavelength of anapole mode. White dashed arrows depict the orientations of the magnetic field. The *xy* cut plane is located in the middle of the upper dumbbell-perforated gold film. All the geometric parameters are identical to those in Fig. 2

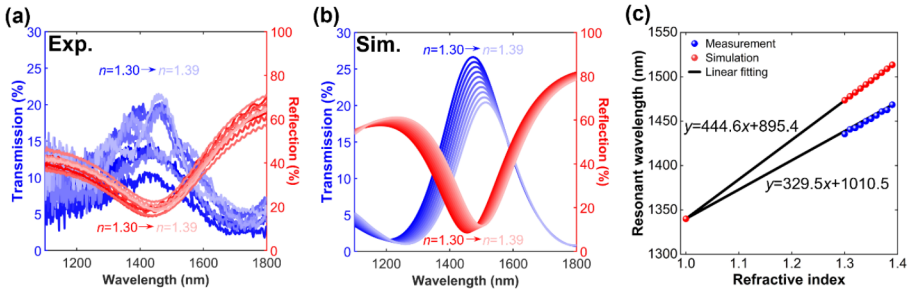

Fig. 4 Refractive index sensing application of the plasmonic anapole metamaterial. (a) Measured and (b) simulated transmission and reflection spectra with variable ambient refractive index from 1.30 to 1.39 with a step of 0.01. Dark (light) blue and red correspond to transmission and reflection at refractive index $n = 1.30$ (1.39). (c) The resonant wavelengths of the anapole mode from experimental and simulation results as functions of the ambient refractive index. The black solid lines represent the linear fitting results

resonator, which simultaneously inherits the properties of both dumbbell-perforated gold film and vertical split-ring resonator.

We now turn our attention to the sensitivity of metamaterial's resonant mode to the ambient refractive index. In the case of the metamaterial considered here, the toroidal dipole moment is parallel to the direction of the incident electric field, which offers stronger interactions between light and matter than that is perpendicular [24, 25]. Moreover, according to the field distributions in Fig. 3e, the electric hotspot is exposed to the environment, resulting in a strong interaction between hotspot and sensing medium and subsequently a high sensitivity to the ambient refractive index variations. In contrast, for dielectric anapole metamaterials and metasurfaces reported in the literature, the

electromagnetic field remains hidden within the dielectric, limiting the practical utility of these devices [45, 46].

Benefiting from the effective coupling between two components and the subsequent anapole mode, the maximum electric field enhancement factor $|E/E_0| = 15.2$ in yz plane is larger than those of only dumbbell-perforated gold film ($|E/E_0| = 10.6$) and only vertical split-ring resonator ($|E/E_0| = 3.3$). Moreover, as shown in Fig. 3b, the simulated line width of the plasmonic anapole metamaterial is reduced to 295 nm, which is smaller than those of only dumbbell-perforated gold film (1137 nm) and vertical split-ring resonator (404 nm). These advantages are expected to efficiently promote sensing performance. It should be noted that the magnetic field enhancement $|H/H_0| = 11.9$ is smaller than that of only the vertical split-ring resonator because of the unavoidable influence of the upper dumbbell-perforated gold film. Since the magnetic hotspot is located in the spin on glass layer, its impact on sensitivity will be reduced.

To investigate and examine the sensing performance of the plasmonic anapole metamaterial, we deposit the oil with a refractive index from 1.30 to 1.39 with a step of 0.01 onto the sample. Figure 4a shows the measured transmission and reflection spectra with variable ambient refractive index. With the ambient refractive index varying from 1.30 to 1.39, the measured resonant wavelength redshifts from 1435.5 to 1468.5 nm. The simulated result in Fig. 4b is in good agreement with the measured one, indicating a redshift of the resonant wavelength from 1473.5 to 1513.4 nm without changing the line shape. These two results both show the linear relationship between the resonant wavelength and refractive index, which is consistent with the theoretical model [47]. The small difference between these two results is due to the roughness of the sample. As a key performance of the sensor, the sensitivity $\Delta\lambda/\Delta n$ defined as the spectral shift per refractive index unit (RIU) is studied in Fig. 4c. By employing a linear fitting, the sensitivities of measurement and simulation results are around 330 nm/RIU and 445 nm/RIU, respectively, which are comparative to conventional plasmonic refractive index sensors by LSPR [5, 13, 15, 48]. The proposed anapole metamaterial sensor can acquire an effective transmission channel due to the nonradiative property, which is beneficial to practical low-loss meta-devices. Considering the infrared spectrometer resolution of around 28.7 pm, the experimental detection limit $\Delta n_{\text{limit}} = \Delta\lambda_{\text{limit}}/\text{Sensitivity} = 8.7 \times 10^{-5}$ RIU can be obtained.

In addition, to analyze the influence of ambient refractive index on the multipole contribution and thus the anapole mode, the multipole decompositions and phases of electric dipole and toroidal dipole moments with different ambient refractive index are given in the Supplementary Information. The contributions of electric dipole and toroidal dipole moments and their phase differences keep nearly constant except for a redshift, which demonstrates that the proposed plasmonic anapole metamaterial can work in a wide range of refractive index and provides a novel method of adjusting the ambient refractive index to flexibly manipulate the anapole mode.

Conclusion

To conclude, we have demonstrated the plasmonic metamaterial with anapole response and its application in refractive index sensing. By analyzing the spectra, multipole decompositions and field distributions of the upper dumbbell-perforated gold film and the lower vertical split-ring resonator, we demonstrate that the anapole mode cannot be

directly excited in a single component, while they can provide efficient electric dipole and toroidal dipole moments and effectively couple with each other, which are desirable for the anapole response. After the combination of these two components, an anapole mode at around 1340 nm with a stronger electric field enhancement factor of 15.2 and a narrower line width of 295 nm can be achieved. Benefiting from these characteristics, the sensitivities of the plasmonic anapole-based refractive index sensor are 330 nm/RIU and 445 nm/RIU in experiment and simulation, respectively. Considering the infrared spectrometer resolution, the experimental detection limit of 8.7×10^{-5} RIU is obtained. Apart from sensing application, this work opens new paths for manipulating the plasmonic anapole mode by varying ambient refractive index and facilitates its applications in spectroscopy and optical nonlinearity.

Methods

Metamaterial nanofabrication

First, a ZEP520A layer was spin-coated at 4000 rpm onto a fused silica substrate and baked for 5 min at 180 °C. An Espacer layer was spin-coated at 1500 rpm onto the ZEP520A layer to reduce the positional error during the e-beam exposure. The base rod and two prongs of vertical split-ring resonator were fabricated by successive two e-beam exposures and lift-off processes. Then, a spin on glass layer isolating the dumbbell-perforated gold film and vertical split-ring resonator was spin-coated at 3000 rpm onto the fused silica substrate with fabricated vertical split-ring resonator and baked for 3 min at 200 °C. Its thickness of 135 nm was acquired by the reactive ion etching (RIE). Last, 30 nm gold films were deposited by RF sputter, and the antietch layer (ZEP520A) was spin-coated onto the gold film. The dumbbell-shaped holes in the same area were processed by e-beam exposure and fabricated by the RIE process.

Optical measurement

Bruker VERTEX 70 Fourier-transform infrared spectrometer equipped with Bruker HYPERION 2000 infrared microscope was exploited to measure the spectrum data. An aperture was employed to collect the incidence to a square area of about 150×150 μm^2, similar to the size of the fabricated sample. The transmission and reflection spectra were normalized by those of the fused silica substrate and the gold mirror. Refractive index sensing is performed by placing a drop of oil with a certain refractive index (Cargille oils Series AAA), measuring the transmission and reflection spectra of the metamaterial, rinsing the sample in methanol, drying, and repeating again. The thickness of oil layer is more than 100 μm to ensure the sample area can be entirely covered, which is far larger than sample thickness and wavelength, and the influence of oil thickness can thus be ignored.

Numerical simulation

Electromagnetic responses of the metamaterial were numerically simulated by commercial software COMSOL Multiphysics based on the finite element method. Perfectly matched layers (PMLs) at the top and bottom of the metamaterial were used to truncate the open space. Periodic boundary conditions were employed in x and y directions to simulate the periodic array. Due to the large thickness of the oil layer, it is simulated as the background media above the metamaterial. The maximum mesh element size is less

than 1/10 of the wavelength, and the resolution of narrow regions is larger than 2. The refractive indexes of the fused silica substrate and spin on glass layer were 1.4584 and 1.41, respectively. The permittivity of gold was described by the Lorentz-Drude model with a plasma frequency of 8.997 eV and a damping coefficient of 0.07 eV. As the wavelength is shorter than 1800 nm, an additional imaginary part of the permittivity of gold was involved to consider the higher experimental loss at the shorter wavelength (see Supplementary Information).

Abbreviations

SPP	surface plasmon polariton.
LSPR	localized surface plasmon resonance.
FOM	figure-of-merit.
ED	electric dipole.
TD	toroidal dipole.
MQ	magnetic quadrupole.
MD	magnetic dipole.
EQ	electric quadrupole.
RIU	refractive index unit.
RIE	reactive ion etching.
PML	perfectly matched layer.

Supplementary Information

The online version contains supplementary material available at https://doi.org/10.1186/s43074-022-00069-x.

Supplementary Material 1

Acknowledgements

The authors acknowledge support from University of Southampton, Nanyang Technological University, and City University of Hong Kong.

Authors' contributions

J.Y., J.Y.O., V.S., N.I.Z, and D.P.T. conceived the idea and designed the experiments. J.Y., V.S. M.K.C., and H.Y.K. designed the samples and performed the theoretical simulations. J.Y.O., V.S., and H.Y.K. developed the technology and fabricated the samples. J.Y.O. and H.Y.K. performed the inspections of the samples and the optical measurements. J.Y. and M.K.C. performed the data analysis. J.Y., J.Y.O., V.S., M.K.C., N.I.Z, and D.P.T. discussed and prepared the manuscript, and all authors reviewed it. N.I.Z and D.P.T. initiated and supervised the research. All authors read and approved the final proof.

Funding

This work is supported by the UK Engineering and Physical Science Research Council (grants EP/M009122/1 and EP/T02643X/1), the Royal Society (grant IEC/R3/170092), the European Research Council (Advanced Grant No. FLEET-786851), the Singapore Ministry of Education (N.I.Z.; grant MOE2016-T3-1-006), the University Grants Committee / Research Grants Council of the Hong Kong Special Administrative Region, China (Project No. AoE/P-502/20 and GRF Project: 15303521), the Shenzhen Science and Technology Innovation Commission (Grant No. SGDX20190816232811 69), the Department of Science and Technology of Guangdong Province (2020B1515120073), and the City University of Hong Kong (Grant No. 9380131).

Data Availability

The data that support the findings of this study are openly available in University of Southampton ePrints research repository at https://doi.org/10.5258/SOTON/D2387.

Declarations

Competing interests

The authors declare that they have no competing interests.

Author details

[1]Department of Electrical Engineering, City University of Hong Kong, Kowloon, Hong Kong SAR, China
[2]Optoelectronics Research Centre, Centre for Photonic Metamaterials, University of Southampton, SO17 1BJ Highfield, Southampton, UK
[3]Centre for Biosystems, Neuroscience, and Nanotechnology, City University of Hong Kong, Kowloon, Hong Kong SAR, China
[4]The State Key Laboratory of Terahertz and Millimeter Waves, City University of Hong Kong, Kowloon, Hong Kong SAR, China
[5]Centre for Disruptive Photonic Technologies, SPMS, Nanyang Technological University, 637371 Singapore, TPI, Singapore

Received: 29 July 2022 / Revised: 6 September 2022 / Accepted: 16 September 2022

Published online: 14 October 2022

References

1. Altug H, Oh SH, Maier SA, Homola J. Advances and applications of nanophotonic biosensors. Nat Nanotechnol. 2022;17:5–16.
2. Tseng ML, Jahani Y, Leitis A, Altug H. Dielectric Metasurfaces Enabling Advanced Optical Biosensors. ACS Photonics. 2020;8:47–60.
3. Ahmadivand A, Gerislioglu B. Photonic and Plasmonic Metasensors. Laser Photonics Rev. 2021;16:2100328.
4. Park J-H, Ndao A, Cai W, Hsu L, Kodigala A, Lepetit T, Lo Y-H, Kanté B. Symmetry-breaking-induced plasmonic exceptional points and nanoscale sensing. Nat Phys. 2020;16:462–8.
5. Nugroho FAA, Albinsson D, Antosiewicz TJ, Langhammer C. Plasmonic Metasurface for Spatially Resolved Optical Sensing in Three Dimensions. ACS Nano. 2020;14:2345–53.
6. You JW, Ma Q, Lan Z, Xiao Q, Panoiu NC, Cui TJ. Reprogrammable plasmonic topological insulators with ultrafast control. Nat Commun. 2021;12:5468.
7. Liu C, Ma Q, Luo ZJ, Hong QR, Xiao Q, Zhang HC, Miao L, Yu WM, Cheng Q, Li L. A programmable diffractive deep neural network based on a digital-coding metasurface array. Nat Electron. 2022;5:113–22.
8. Allison G, Sana AK, Ogawa Y, Kato H, Ueno K, Misawa H, Hayashi K, Suzuki H. A Fabry-Perot cavity coupled surface plasmon photodiode for electrical biomolecular sensing. Nat Commun. 2021;12:6483.
9. Shen Y, He K, Zou Q, Xing S, Huang J, Zheng M, She X, Jin C. Ultrasmooth Gold Nanogroove Arrays: Ultranarrow Plasmon Resonators with Linewidth down to 2 nm and Their Applications in Refractive Index Sensing. Adv Funct Mater. 2021;32:2108741.
10. Kabashin AV, Evans P, Pastkovsky S, Hendren W, Wurtz GA, Atkinson R, Pollard R, Podolskiy VA, Zayats AV. Plasmonic nanorod metamaterials for biosensing. Nat Mater. 2009;8:867–71.
11. Sreekanth KV, Alapan Y, ElKabbash M, Ilker E, Hinczewski M, Gurkan UA, De Luca A, Strangi G. Extreme sensitivity biosensing platform based on hyperbolic metamaterials. Nat Mater. 2016;15:621–7.
12. Xu Y, Bai P, Zhou X, Akimov Y, Png CE, Ang LK, Knoll W, Wu L. Optical Refractive Index Sensors with Plasmonic and Photonic Structures: Promising and Inconvenient Truth. Adv Opt Mater. 2019;7:1801433.
13. Wu PC, Liao CY, Chen J-W, Tsai DP. Isotropic Absorption and Sensor of Vertical Split-Ring Resonator. Adv Opt Mater. 2017;5:1600581.
14. Gerislioglu B, Dong L, Ahmadivand A, Hu H, Nordlander P, Halas NJ. Monolithic Metal Dimer-on-Film Structure: New Plasmonic Properties Introduced by the Underlying Metal. Nano Lett. 2020;20:2087–93.
15. Wu PC, Sun G, Chen WT, Yang K-Y, Huang Y-W, Chen Y-H, Huang HL, Hsu W-L, Chiang HP, Tsai DP. Vertical split-ring resonator based nanoplasmonic sensor. Appl Phys Lett. 2014;105:033105.
16. Ahmed R, Ozen MO, Karaaslan MG, Prator CA, Thanh C, Kumar S, Torres L, Iyer N, Munter S, Southern S, Henrich TJ, Inci F, Demirci U. Tunable Fano-Resonant Metasurfaces on a Disposable Plastic-Template for Multimodal and Multiplex Biosensing. Adv Mater. 2020;32:1907160.
17. Liang Y, Koshelev K, Zhang F, Lin H, Lin S, Wu J, Jia B, Kivshar Y. Bound States in the Continuum in Anisotropic Plasmonic Metasurfaces. Nano Lett. 2020;20:6351–6.
18. Chen H, Wang H, Wong KY, Lei D. High-Q localized surface plasmon resonance based on bound states in the continuum for enhanced refractive index sensing. Opt Lett. 2022;47:609–12.
19. Cetin AE, Altug H. Fano resonant ring/disk plasmonic nanocavities on conducting substrates for advanced biosensing. ACS Nano. 2012;6:9989–95.
20. Wang J, Kühne J, Karamanos T, Rockstuhl C, Maier SA, Tittl A. All-Dielectric Crescent Metasurface Sensor Driven by Bound States in the Continuum. Adv Funct Mater. 2021;31:2104652.
21. Zhou Y, Guo Z, Zhao X, Wang F, Yu Z, Chen Y, Liu Z, Zhang S, Sun S, Wu X. Dual-Quasi Bound States in the Continuum Enabled Plasmonic Metasurfaces. Adv Opt Mater. 2022:2200965.
22. Baryshnikova KV, Smirnova DA, Luk'yanchuk BS, Kivshar YS. Optical Anapoles: Concepts and Applications. Adv Opt Mater. 2019;7:1801350.
23. Yang Y, Bozhevolnyi SI. Nonradiating anapole states in nanophotonics: from fundamentals to applications. Nanotechnology. 2019;30:204001.
24. Fedotov VA, Rogacheva AV, Savinov V, Tsai DP, Zheludev NI. Resonant transparency and non-trivial non-radiating excitations in toroidal metamaterials. Sci Rep. 2013;3:2967.
25. Wu PC, Liao CY, Savinov V, Chung TL, Chen WT, Huang YW, Wu PR, Chen YH, Liu AQ, Zheludev NI, Tsai DP. Optical Anapole Metamaterial. ACS Nano. 2018;12:1920–7.
26. Miroshnichenko AE, Evlyukhin AB, Yu YF, Bakker RM, Chipouline A, Kuznetsov AI, Luk'yanchuk B, Chichkov BN, Kivshar YS. Nonradiating anapole modes in dielectric nanoparticles. Nat Commun. 2015;6:8069.
27. Semmlinger M, Zhang M, Tseng ML, Huang TT, Yang J, Tsai DP, Nordlander P, Halas NJ. Generating Third Harmonic Vacuum Ultraviolet Light with a TiO2 Metasurface. Nano Lett. 2019;19:8972–8.
28. Yao J, Li B, Cai G, Liu QH. Doubly mirror-induced electric and magnetic anapole modes in metal-dielectric-metal nanoresonators. Opt Lett. 2021;46:576–9.
29. Gurvitz EA, Ladutenko KS, Dergachev PA, Evlyukhin AB, Miroshnichenko AE, Shalin AS. The High-Order Toroidal Moments and Anapole States in All - Dielectric Photonics. Laser Photonics Rev. 2019;13:1800266.
30. Ospanova AK, Stenishchev IV, Basharin AA. Anapole Mode Sustaining Silicon Metamaterials in Visible Spectral Range. Laser Photonics Rev. 2018;12:1800005.
31. Hernandez-Sarria JJ, Oliveira ON, Mejia-Salazar JR. Toward Lossless Infrared Optical Trapping of Small Nanoparticles Using Nonradiative Anapole Modes. Phys Rev Lett. 2021;127:186803.
32. Hüttenhofer L, Tittl A, Kühner L, Cortés E, Maier SA. Anapole-Assisted Absorption Engineering in Arrays of Coupled Amorphous Gallium Phosphide Nanodisks. ACS Photonics. 2021;8:1469–76.
33. Kuznetsov AI, Evlyukhin AB, Gonçalves MR, Reinhardt C, Koroleva A, Arnedillo ML, Kiyan R, Marti O, Chichkov BN. Laser fabrication of large-scale nanoparticle arrays for sensing applications. ACS Nano. 2011;5:4843–9.

34. Jeong J, Goldflam MD, Campione S, Briscoe JL, Vabishchevich PP, Nogan J, Sinclair MB, Luk TS, Brener I. High Quality Factor Toroidal Resonances in Dielectric Metasurfaces. ACS Photonics. 2020;7:1699–707.
35. Wang W, Srivastava YK, Gupta M, Wang Z, Singh R. Photoswitchable Anapole Metasurfaces. Adv Opt Mater. 2021;10:2102284.
36. Liu X, Liu Z, Hua M, Wang L, Wang K, Zhang W, Ning Y, Shi Y, Wang X, Yang F. Tunable Terahertz Metamaterials Based on Anapole Excitation with Graphene for Reconfigurable Sensors. ACS Appl Nano Mater. 2020;3:2129–33.
37. Savinov V, Papasimakis N, Tsai DP, Zheludev NI. Optical anapoles. Commun Phys. 2019;2:1–4.
38. Wu J, Li Z, Li M, Wang Y. Plasmonic refractive index sensing enhanced by anapole modes in metal-dielectric nanostructure array. J Opt. 2021;23:035002.
39. Kaelberer T, Fedotov V, Papasimakis N, Tsai D, Zheludev N. Toroidal dipolar response in a metamaterial. Science. 2010;330:1510–2.
40. Papasimakis N, Fedotov VA, Savinov V, Raybould TA, Zheludev NI. Electromagnetic toroidal excitations in matter and free space. Nat Mater. 2016;15:263–71.
41. Wu PC, Chen WT, Yang K-Y, Hsiao CT, Sun G, Liu AQ, Zheludev NI, Tsai DP. Magnetic plasmon induced transparency in three-dimensional metamolecules. Nanophotonics. 2012;1:131–8.
42. Chen CC, Hsiao CT, Sun S, Yang K-Y, Wu PC, Chen WT, Tang YH, Chau Y-F, Plum E, Guo G-Y, Zheludev NI, Tsai DP. Fabrication of three dimensional split ring resonators by stress-driven assembly method. Opt Express. 2012;20:9415–20.
43. Chan H-C, Sun S, Guo G-Y. Near-infrared left-handed metamaterials made of arrays of upright split-ring pairs. J Phys D: Appl Phys. 2018;51:265103.
44. Tsai WY, Chung TL, Hsiao HH, Chen JW, Lin RJ, Wu PC, Sun G, Wang CM, Misawa H, Tsai DP. Second Harmonic Light Manipulation with Vertical Split Ring Resonators. Adv Mater. 2019;31:1806479.
45. Zanganeh E, Evlyukhin A, Miroshnichenko A, Song M, Nenasheva E, Kapitanova P. Anapole Meta-Atoms: Nonradiating Electric and Magnetic Sources. Phys Rev Lett. 2021;127:096804.
46. Yang Y, Zenin VA, Bozhevolnyi SI. Anapole-Assisted Strong Field Enhancement in Individual All-Dielectric Nanostructures. ACS Photonics. 2018;5:1960–6.
47. Zhu J, Zhang L, Jiang S, Ou J-Y, Liu QH. Selective light trapping of plasmonic stack metamaterials by circuit design. Nanoscale. 2020;12:2057–62.
48. Ray D, Raziman TV, Santschi C, Etezadi D, Altug H, Martin OJF. Hybrid Metal-Dielectric Metasurfaces for Refractive Index Sensing. Nano Lett. 2020;20:8752–9.

Publisher's Note